A New Piezoelectric Energy Harvesting Design Concept: Multimodal Energy Harvesting Skin

Soobum Lee and Byeng D. Youn

Abstract—This paper presents an advanced design concept for a piezoelectric energy harvesting (EH), referred to as multimodal EH skin. This EH design facilitates the use of multimodal vibration and enhances power harvesting efficiency. The multimodal EH skin is an extension of our previous work, EH skin, which was an innovative design paradigm for a piezoelectric energy harvester: a vibrating skin structure and an additional thin piezoelectric layer in one device. A computational (finite element) model of the multilayered assembly—the vibrating skin structure and piezoelectric layer—is constructed and the optimal topology and/or shape of the piezoelectric layer is found for maximum power generation from multiple vibration modes. A design rationale for the multimodal EH skin was proposed: designing a piezoelectric material distribution and external resistors. In the material design step, the piezoelectric material is segmented by inflection lines from multiple vibration modes of interests to minimize voltage cancellation. The inflection lines are detected using the voltage phase. In the external resistor design step, the resistor values are found for each segment to maximize power output. The presented design concept, which can be applied to any engineering system with multimodal harmonic-vibrating skins, was applied to two case studies: an aircraft skin and a power transformer panel. The excellent performance of multimodal EH skin was demonstrated, showing larger power generation than EH skin without segmentation or unimodal EH skin.

I. INTRODUCTION

RESEARCH into energy harvesting (EH) has resulted in the creation of wireless electrical devices, such as wireless sensors, which are powered by collecting ambient, otherwise wasted, energy. This EH technology is in high demand because wireless sensors are increasingly used in the areas of structural health monitoring (SHM), building automation, etc. Battery-powered wireless sensors, can be troublesome because of the limited lifespan and replacement cost ($80 to 500 including labor [1]) of batteries, especially when the sensors are installed in remote locations. This issue has motivated the rapid growth of the EH field.

Vibration is one of the most commonly available forms of ambient energy, found in civil structures, machines, the human body, etc. Various vibration sources with their maximum acceleration magnitude and frequency range were well listed by Roundy *et al.* [2]. Among several energy conversion principles for converting vibration energy, piezoelectricity is known to be the most efficient [1], [3], simplest, and most practical methods of conversion [3]–[5]. Piezoelectric materials include lead zirconate titanate (PZT), zinc oxide (ZnO), polyvinylidene difluoride (PVDF), lead magnesium niobate-lead titanate (PMN-PT) [6], and polypropylene (PP) polymer. Even though PMN-PT is known to have a large coupling coefficient, the price is very high and the availability in commercial market is still low, to the authors' knowledge. Among the remainder, PZT is known to possess the best conversion efficiency [4]. PZT is therefore chosen for implementing harvesters throughout this paper.

Some ambient vibration sources from machinery and human movement have been utilized for piezoelectric EH. Elvin *et al.* [7] proposed a possible implementation of self-powered damage detection using PVDF in a construction site: a time-varying load from a roller cart can generate sufficient mechanical strains for EH. Nuffer and Bein [8] discussed an EH application for monitoring transportation (e.g., vehicle) by using piezoelectric EH to power wireless sensors. Some case studies of EH from vehicle engine vibration and bridge vibration can be found on the AmbioSystem website [9]. Granstrom *et al.* [10] developed a piezoelectric polymer backpack strap which generated electrical energy from the oscillating tension of the strap during walking. Leland *et al.* [11] mounted an EH device to generate electricity from vibrations in a staircase and obtained output of approximately 30 μW. Shoe-mounted EH is another example of EH which utilizes human movement—pressure by heel strikes [12], [13]. Jeon *et al.* [12] developed a thin-film PZT power generator for MEMS devices, utilizing the d_{33} mode to yield about 1 μW. The current state-of-art can barely generate electrical power to operate wireless sensor nodes and small electronics [13]–[15] even though extensive research has been done for the last two decades.

Previous studies of piezoelectric EH technology have been focused on designing EH devices (shape, location, material), electric circuits, or both. Some researchers found that a trapezoidal cantilever shape is more efficient than a rectangular cantilever shape because of the uniformly large strain at every point on the beam surface [3],
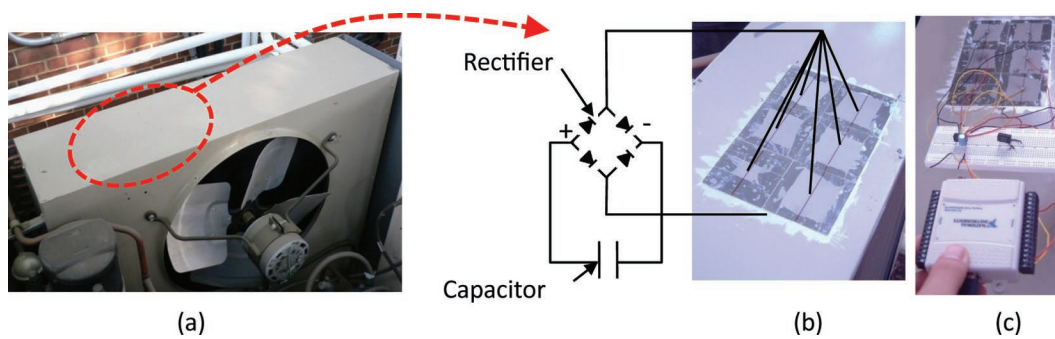
Fig. 1. EH skin on (a) an outdoor condensing unit, (b) EH skin implementation, and (c) power measurement.

[16], [17]. Zheng et al. [18] employed topology optimization for designing an optimal piezoelectric EH cantilever beam by maximizing an energy conversion factor. Even though their contributions were unique, consideration of a static load is conceived to be their limitation. Other limitations of this study, including electric circuitry, were discussed by Silva [19]. Erturk and Inman [20] noted several oversimplified and incorrect physical assumptions from previous research into a cantilever EH device. They investigated the problems related to two modeling topics: single degree-of-freedom modeling and distributed parameter modeling. Corrections to the models were provided with improved models and examples.

Appropriate material selection is also an important factor for EH devices. Kim et al. [21] summarized various kinds of piezoelectric materials and compared their energy conversion performance, operating temperature range, and mode to be utilized (e.g., d_{31}, d_{33}). Shen et al. [22] experimentally compared EH performance of three kinds of piezoelectric material (piezoelectric ceramic, fiber, and polymer). A new conceptual design of EH cantilever was proposed by Lee et al. [23] to utilize multiple vibration modes, enabled by segmented piezoelectric material on a cantilever. To enhance power generation capability, Tadesse et al. [24] implemented a hybrid EH device which involved piezoelectric and electromagnetic conversion principles. A cantilever beam with a tip magnet and PZT patches was designed to produce power from multiple excitation frequencies. Other researchers have looked into designing electrical circuitry for better energy harvesting performance. Kasyap et al. [25] developed the fly-back converter circuit, with which impedance could be modified to match that of the piezoelectric device. Ottman et al. [26] studied the use of an adaptive step-down dc-dc converter to maximize the power output from a piezoelectric device. Meninger et al. [27] developed an energy harvesting system, with which the conversion process can be modified through the use of an additional capacitor to provide maximal energy transfer. Guan and Liao [28] studied the efficiencies of the energy harvesting circuits considering the storage device voltages. Recently, Rupp et al. [29] developed a design method for a multilayer shell-type piezoelectric EH system, in which the topology of piezoelectric material and external resistance were simultaneously considered as design factors. Recent studies on piezoelectric EH devices are well summarized in the review articles [17], [30], [31].

Even though most piezoelectric EH devices take a form of cantilever, this form has some drawbacks from a practical point of view. First, the cantilever EH device requires more space because of a bulky proof mass and additional clamping part. Second, the cantilever EH device must be protected from dirt, moisture, and other environmental harm; it is suggested that the cantilever EH device be kept inside housing or vibrating structure for its protection. Third, a great deal of vibration energy can be lost when clamping conditions become loosened after long-term exposure to vibration. The disadvantages of the cantilever design motivated the proposition of an innovative and practical EH design called an energy-harvesting skin [32]. In the EH skin, thin piezoelectric patches were directly attached onto a vibrating shell structure to harvest electric power in an attempt to overcome the drawbacks of the cantilever EH device. The vibrating skin in various kinds of engineering systems (e.g., vehicles, home appliances, HVAC facilities, etc.) takes the role of a substrate. A practical implementation of this design concept can be found in one of our previous works, as shown in Fig. 1 [32]: an EH skin using an outdoor condensing unit's vibration. Rectangular PZT patches were attached on the top of the outdoor unit using epoxy and wired with a rectifier and capacitor to generate about 3.7 mW. This simple embodiment enables an EH device without additional fixture or protection housing as long as the piezoelectric patches are placed inside the skin (e.g., under the outdoor unit skin). However, in this previous work, only a single vibration mode at harmonic frequency around 60 Hz was utilized; the other multiple harmonic modes (e.g., 120, 180 Hz) were still wasted. For this reason, this harvester is referred as a unimodal EH skin. A design methodology to use multiple harmonic vibration modes is therefore required to design a device which may harvest more power.

This paper proposes an advanced EH skin design concept, called multimodal EH skin, which uses multimodal vibration and enhances the energy harvesting capability. The proposed design methodology was applied to two case studies: an aircraft skin and a power transformer, and it
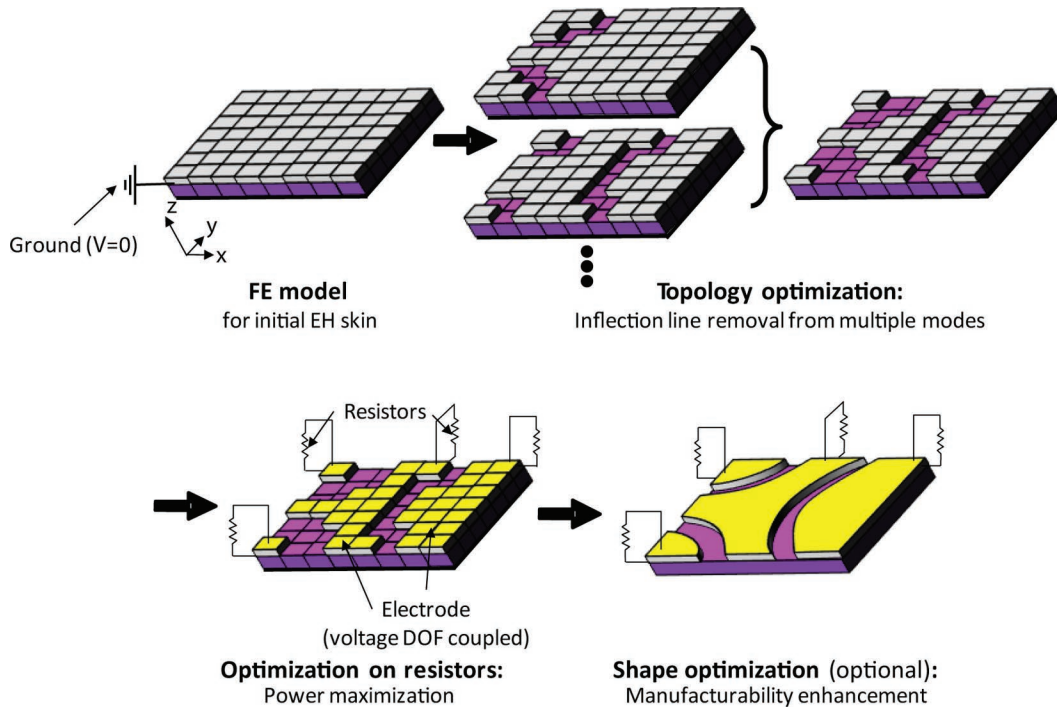
Fig. 2. Design procedure for multimodal EH skin.

was found that the multimodal energy harvesting skin produced more energy than the unimodal EH skin.

The paper is organized as follows: the proposed multimodal EH skin design methodology is presented in Section II, and the case studies for an aircraft skin vibration and a power transformer vibration follow in Section III.

II. DESIGN PROCESS OF MULTIMODAL ENERGY HARVESTING SKIN

This section explains the design process for the multimodal EH skin. The design process consists of two major steps (see Fig. 2): design of the piezoelectric material distribution and design of the external resistors. First, topology optimization determines an optimal piezoelectric material distribution by removing the materials along inflection lines from multiple vibration modes (in Fig. 2). The layout of the inflection lines can be found using the voltage phase angle (see Section II-A). An additional shape optimization (SO) step can be performed to make smooth boundaries and enhance manufacturability. Second, after the material design, the external resistor values for each segment are found for power maximization.

A. Designing a Piezoelectric Material Distribution

This paper uses harmonic response analysis (ANSYS, ANSYS Inc., Canonsburg, PA), which solves the time-dependent equation of motion for linear structures under steady-state vibration (vibrating at f_e hertz). If we consider a general equation of motion for a piezoelectric coupled-field structure after the application of the varia-

tional principle and finite element discretization [33], the coupled finite element matrix equation is

$$\begin{bmatrix} \mathbf{M} & \mathbf{0} \\ \mathbf{0} & \mathbf{0} \end{bmatrix} \begin{Bmatrix} \{\ddot{u}\} \\ \{\ddot{V}\} \end{Bmatrix} + \begin{bmatrix} \mathbf{C} & \mathbf{0} \\ \mathbf{0} & \mathbf{0} \end{bmatrix} \begin{Bmatrix} \{\dot{u}\} \\ \{\dot{V}\} \end{Bmatrix} + \begin{bmatrix} \mathbf{K} & \mathbf{K}^z \\ \mathbf{K}^{z\prime} & \mathbf{K}^d \end{bmatrix} \begin{Bmatrix} \{u\} \\ \{V\} \end{Bmatrix} = \begin{Bmatrix} \{F\} \\ \{L\} \end{Bmatrix}, \tag{1}$$

where $\mathbf{M}$, $\mathbf{C}$, and $\mathbf{K}$ are structural mass, damping, and stiffness matrices, respectively; $\mathbf{K}^z$ is the piezoelectric coupling matrix, $\mathbf{K}^d$ is the dielectric conductivity matrix, $\{u\}$ is the displacement vector, $\{V\}$ is the electrical potential (voltage) vector, and $\{F\}$ and $\{L\}$ are structural and electrical load vectors. The electrical load vector is assumed to be zero in this paper ($\{L\} = \mathbf{0}$): only the structural input loading exists for the design of energy harvester. In the harmonic response analysis, all points in the structure are vibrating at the same known frequency. Therefore the displacements and electrical potential may be defined as

$$\begin{aligned} \{u\} &= \{u_{\max}\}e^{i(\phi+\omega t)} = \{u_{\max}(\cos\phi + i\sin\phi)\}e^{i\omega t} \\ &= [\{u_{\mathrm{re}}\} + i\{u_{\mathrm{im}}\}]e^{i\omega t} \\ \{V\} &= \{V_{\max}\}e^{i(\phi+\omega t)} = \{V_{\max}(\cos\phi + i\sin\phi)\}e^{i\omega t} \\ &= [\{V_{\mathrm{re}}\} + i\{V_{\mathrm{im}}\}]e^{i\omega t}, \end{aligned} \tag{2}$$

where $\{u_{\max}\}$ ($\{V_{\max}\}$) is the maximum displacement (maximum electrical potential), ϕ is the phase angle, ω ($= 2\pi f_e$) is the imposed excitation frequency in radians per second, and $\{u_{\mathrm{re}}\}$ and $\{u_{\mathrm{im}}\}$ ($\{V_{\mathrm{re}}\}$ and $\{V_{\mathrm{im}}\}$) are real and imaginary displacement (electrical potential) vectors, respectively. The force vector can be specified analogously as
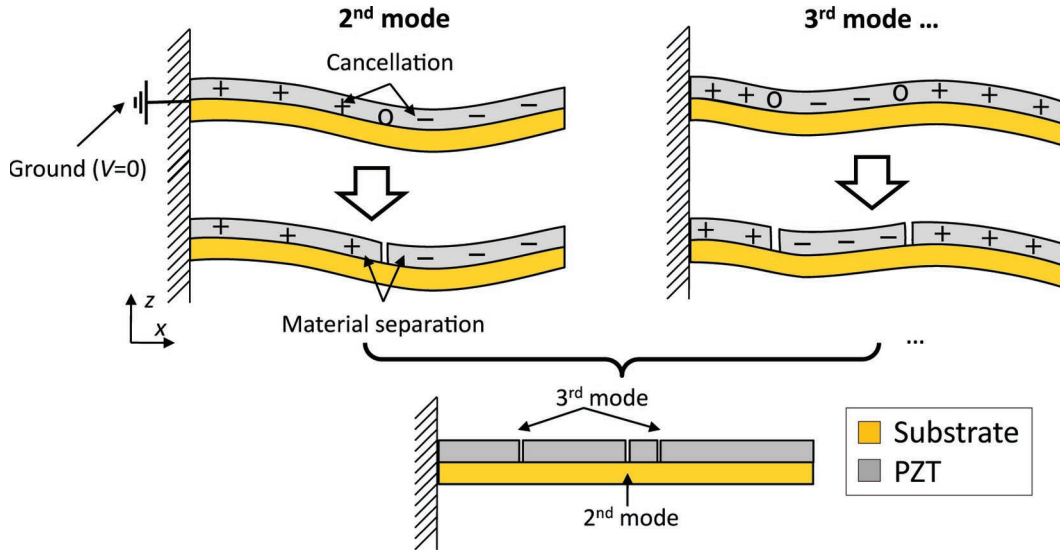
Fig. 3. Prevention of cancellation effect by removing piezoelectric material at inflection points (no cancellation occurs in the first mode).

$$\{F\} = \{F_{\max}\}e^{i(\phi+\omega t)} = \{F_{\max}(\cos\phi + i\sin\phi)\}e^{i\omega t}$$
$$= [\{F_{\mathrm{re}}\} + i\{F_{\mathrm{im}}\}]e^{i\omega t}. \tag{3}$$

Eq. (1) can be rewritten by substituting (2) and (3) and cancelling $e^{i\omega t}$ as

$$\left(-\omega^2\begin{bmatrix} \mathbf{M} & \mathbf{0} \\ \mathbf{0} & \mathbf{0} \end{bmatrix} + i\omega\begin{bmatrix} \mathbf{C} & \mathbf{0} \\ \mathbf{0} & \mathbf{0} \end{bmatrix} + \begin{bmatrix} \mathbf{K} & \mathbf{K}^z \\ \mathbf{K}^{z\,\prime} & \mathbf{K}^d \end{bmatrix}\right)\begin{bmatrix} \{u_{\mathrm{re}}\} + i\{u_{\mathrm{im}}\} \\ \{V_{\mathrm{re}}\} + i\{V_{\mathrm{im}}\} \end{bmatrix}$$
$$= \begin{bmatrix} \{F_{\mathrm{re}}\} + i\{F_{\mathrm{im}}\} \\ \mathbf{0} \end{bmatrix}. \tag{4}$$

After solving this equation, the complex electrical potential (as well as the displacement) can be expressed in terms of maximum amplitude and phase angle:

$$\{V_{\mathrm{re}}\} + i\{V_{\mathrm{im}}\} = \{V_{\max}(\cos\phi + i\sin\phi)\}$$
$$V_{\max} = \sqrt{V_{\mathrm{re}}^2 + V_{\mathrm{im}}^2}, \quad \phi = \tan^{-1}\frac{V_{\mathrm{im}}}{V_{\mathrm{re}}}. \tag{5}$$

The objective of topological design proposed in this paper is to find the piezoelectric material distribution so that the voltage phase in (5) is almost identical in the material. Fig. 3 illustrates how the topological design is obtained using the phase angle in (5). This figure shows a 2-D unimorph cantilever for better understanding, but the method can be easily extended to 3-D thin vibrating structures.

Suppose the first three vibration modes are to be utilized for energy harvesting, using the d_{31} effect. One may think that the amount of piezoelectric material is proportional to the power generation and want to cover the whole surface of the vibrating structure with piezoelectric material, but in this case the power is not generated at maximum because of the cancellation effect [23], [29], [35].

The cancellation effect refers to the voltage cancellation caused by inconsistent voltage phase in piezoelectric material. Because the generated voltage is proportional to the mechanical strain, the voltage cancellation occurs when the sign of mode-shape curvature changes. Fig. 3 shows an example of this effect from the second and the third vibration modes. Obviously this effect can be minimized by eliminating material around inflection points as shown in the second row of Fig. 3. Considering multiple modes in this example, the final design can be obtained as shown at the bottom of the figure, by eliminating the material at all the inflection points from the second and the third mode (the first mode does not have inflection points in this example).

The same method can be applied in the 3-D skin vibration case. Initially the top surface of a vibrating structure is covered with a thin piezoelectric material layer, and the material is removed along the multiple inflection lines.

The inflection line can be detected by voltage phase angle $[\phi(V)]$ at each node at the top surface level of piezoelectric layer in Fig. 2. Usually a significant change in $\phi(V)$ exists across the inflection line (about 180°). An example of inflection line detection for a skin structure is shown in Fig. 4 which shows the top view (from positive z) of the EH skin in Fig. 2. Suppose that an inflection line, the dotted line in Fig. 4, passes through the center of the element set. By this line the nodes at the top level are divided into two groups in terms of $\phi(V)$: $\phi \approx \theta$ on the right (void circles), $\phi \approx \theta + 180°$ on the left (black circles). To detect and eliminate the inflection lines from multiple excitation frequencies $(f_e{}^i)$, the following procedure is performed:

- Step 1: Perform harmonic analysis using Eq. (1) for a single excitation frequency $(f_e{}^i)$.
- Step 2: For the ith excitation case, visit every FE node at top surface level of piezoelectric and extract the phase (ϕ).
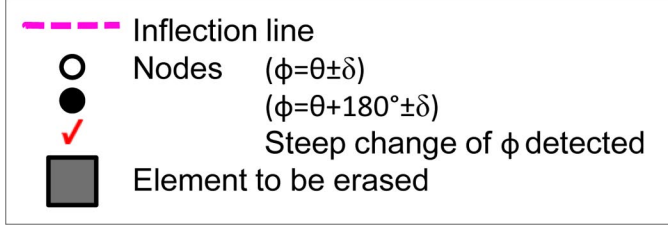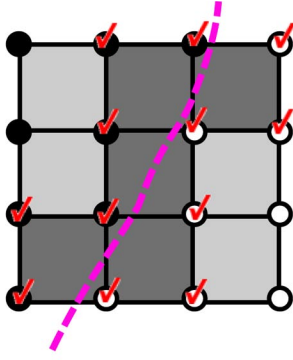
Fig. 4. Inflection line detection (top view of PZT elements).

- Step 3: For every top-level node, check the phase difference with its neighboring 8 nodes
- Step 4: Extract the node set where a significant phase difference is detected (check marks in Fig. 4).
- Step 5: Eliminate the element set composed of the node set in Step 4.
- Step 6: Repeat steps 1–5 for each excitation frequency.

B. Designing External Resistors

After eliminating inflection lines from multiple modes, the total harvested power is estimated through external resistors connected to each segment, as shown in the last panel of Fig. 2. The power measured at the external resistor varies depending on the resistor value, so its optimal value should be found. The shape optimization of the piezoelectric material can be performed additionally to enhance manufacturability. It is noted that the voltage degrees-of-freedom (DOFs) at the top level of the piezoelectric material model are coupled to represent the electrode at each segment.

The design task for finding the optimal external resistor values at each segment (R) and shape design variables (dv) is formulated as

$$\max \sum_n \sum_j P_{nj}(R_j, \mathrm{dv}_k), \qquad (6)$$

where n is the number of multiple harmonic vibration modes, P_{nj} is the power at the jth segment under nth mode excitation, R_j is the resistor at jth segment, and dv_k is the kth shape design variable after the parameterization of the segmented model (See Section III-A-4 for an example of parameterization). The initial values of R_j for the optimization were chosen as

$$R_j = \frac{1}{2\pi f_\mathrm{e} C_j} = \frac{1}{2\pi f_\mathrm{e} \left(\varepsilon_0 \varepsilon \frac{A_j}{d} \right)}, \qquad (7)$$

where C_j is the capacitance of the jth segment, ε is the permittivity of PZT ($\varepsilon_{33}{}^T = 1700$), ε_0 is the vacuum permittivity, A_j is the area of jth segment, and d is the PZT thickness. R_j in this equation had been known as the optimal resistance for maximum power generation [36]–[38]. However, Erturk and Inman [39] commented that this resistance value is erroneous because of the oversimplified analytical modeling in some previous studies (e.g., on piezoelectric coupling in the beam equation). In this paper, (7) was used to provide a starting point for optimization.

III. DESIGN CASE STUDIES

To prove the excellent performance of the proposed EH skin design method, two design case studies were researched: aircraft skin in Section III-A and a power transformer in Section III-B.

A. Case Study 1: Utilization of Aircraft Skin Vibration

1) Aircraft Vibration Data Measurement: The multimodal vibration data from an aircraft skin (Fig. 5) was used for multimodal EH skin design. This case study was motivated by the need to develop self-powered structural monitoring sensors for aircraft (e.g., for the detection of abnormal deformation of the aircraft's structure). The measurement location is also shown in Fig. 5. The vibration level was measured 12 times and a fast Fourier transformation (FFT) was performed to obtain frequency domain data. Some of the FFT plots are shown in Fig. 6, which shows multiple harmonic resonant peaks around 800, 1500, 2000 Hz, etc. The measurement data from the 12 trials (amplitude and frequency) and their average values are listed in Table I for the first two peaks. Variation of the peak amplitudes and frequencies was observed from the multiple measurements. In this case study, the first two resonant frequency components, the average values for the acceleration peaks (A^1 and A^2) and the corresponding frequencies ($f_\mathrm{e}{}^1$, $f_\mathrm{e}{}^2$ in Table I), were used for the design of multimodal EH skin.

2) Modeling of Local Multilayered Aircraft Skin: In this study, a local section of aircraft skin (about 12.5 × 10.5 cm^2) was modeled for the design of EH skin. Fig. 7 shows the FE model for a multilayered skin in which PZT patches were attached on the top of the aircraft skin (aluminum) to form a unimorph layout.

The local model was defined as a rectangle with 9 rivet joints as shown in Fig. 7. The thicknesses of aluminum and PZT-5A were found from manufacturer's catalogs [40], [41] to be 1.6002 mm and 1.02 mm, respectively.

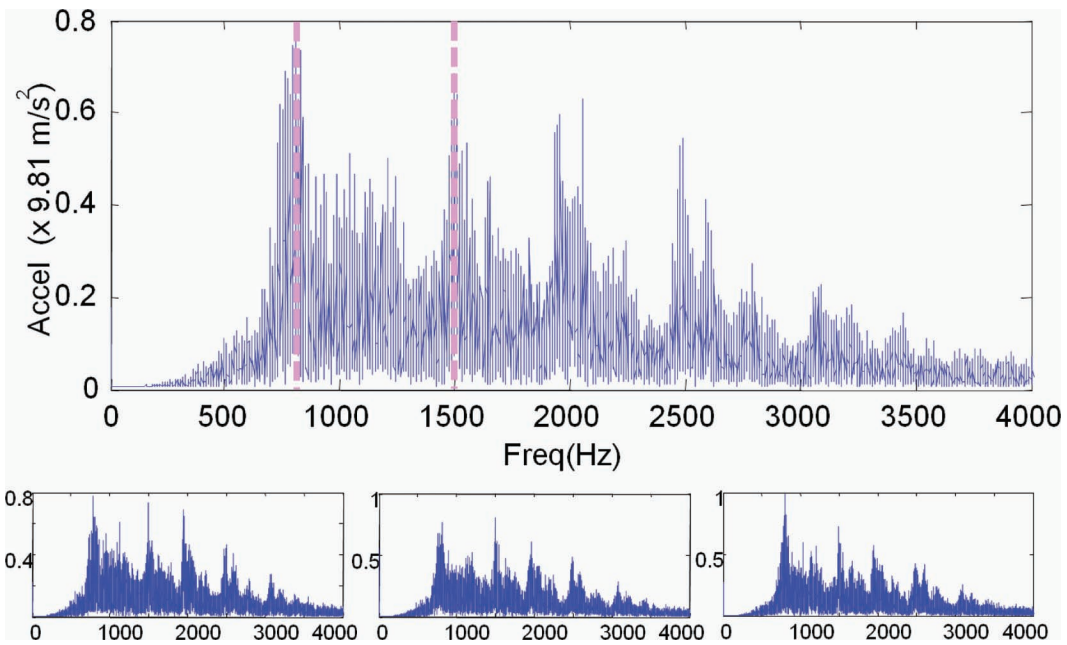Fig. 5. Aircraft skin and measurement location.

Fig. 6. FFT plots of measured vibration amplitude (Trials 1, 5, 9, and 10 in Table I).

TABLE I. Uncertainty on Multimodal Vibration Peak and Frequency.

	1st peak		2nd peak	
Trial	f_e^1, Freq. (Hz)	A^1, Accel. (g)	f_e^2, Freq. (Hz)	A^2, Accel. (g)
1	806.8	0.7624	1499	0.6867
2	816.7	0.7680	1506	0.5993
3	802.4	0.9463	1484	0.7620
4	811.9	1.0060	1511	0.7308
5	820.0	0.7689	1493	0.8074
6	814.1	0.8736	1512	0.6562
7	800.6	0.9903	1502	0.6201
8	779.3	0.9787	1502	0.5878
9	803.5	0.9860	1493	0.7316
10	789.2	0.7813	1502	0.7339
11	790.0	0.9364	1502	0.6746
12	814.1	0.8101	1491	0.7796
Average	804.05	0.8840	1499.75	0.6975
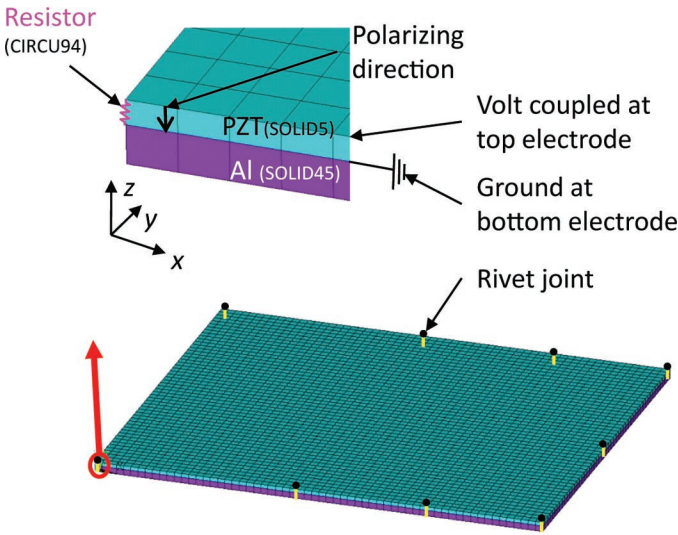
Fig. 7. FE model for a multilayered EH skin.

TABLE II. MATERIAL PROPERTIES FOR AL-7075 AND PZT-5A.

Material	Parameter	Value
Al-7075	ρ_a	2810 kg/m^3
	Y_a	71.7 GPa
	ν_a	0.33
PZT-5A	Mechanical properties	
	ρ_p	7171 kg/m^3
	s_{11}	1.7605E−11 m^2/N
	s_{12}	−5.166E−12 m^2/N
	s_{13}	−7.942E−12 m^2/N
	s_{33}	1.692E−11 m^2/N
	s_{44}	4.275E−11 m^2/N
	s_{66}	4.873E−11 m^2/N
	Coupled and electrical properties	
	d_{31}	−1.539E−10 m/V
	d_{33}	4.114E−10 m/V
	ε_{33}	916.0

$$\min \sum_n (f_r^n(\text{TP}_i) - f_e^n)^2. \tag{8}$$

The PZT patches and substrate were modeled using the SOLID5 and SOLID45 elements in ANSYS (Ansys Inc., Canonsburg, PA), respectively. The SOLID5 element is a 3-D coupled-field solid element which has 4 DOFs at each node: 3 translational DOFs and a voltage DOF. In total, 6448 finite elements were used in this model. The voltage DOFs on the interface with the substrate were grounded. The material properties of aluminum (Al-7075 [42]) and PZT-5A are listed in Table II.

Before carrying out design optimization of the EH skin, the local model was tuned to have the same resonant behavior as shown in Table I, assuming that the multiple resonant peaks in Fig. 6 are generated because of the resonant behavior of the aircraft skin. The resonant frequencies were calculated from modal analysis, in which all DOFs at the 9 rivet joints were fixed. The first two modal shapes are shown in Fig. 8.

Four tuning parameters (TP) were assigned for the frequency-matching procedure as shown in Fig. 9: the length and width of the skin (TP_1, TP_2) and two rivet locations (b and c in Fig. 9) along the horizontal edges (TP_3, TP_4). The design optimization technique was used to match the resonant frequencies of the structure (f_r^n) with f_e^n (in Table I, $n = 1, 2$) as follows:

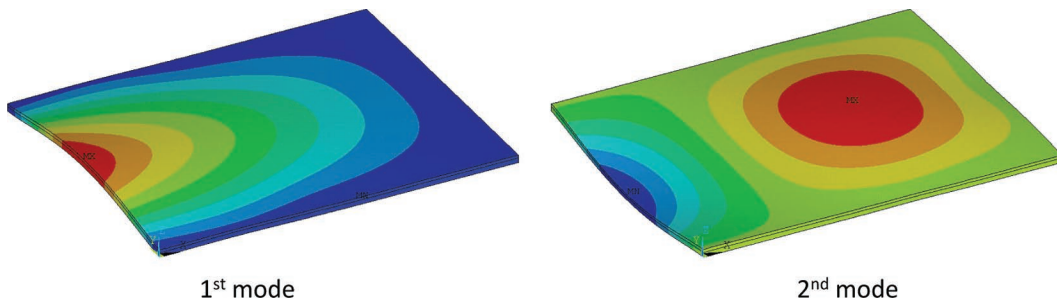We used MATLAB to find the optimal TP_i for the minimization of (8). After the optimization each f_r^n was tuned to f_e^n, and TP_i were found to be 12.47, 10.55, 5.628, and 9.304 cm, respectively.

3) Topological Optimization: Aircraft skin vibration is mainly generated by the regular engine rotation, so this loading condition can be modeled as a sine-sweep acceleration base input. This input can be implemented using the large mass method (LMM). The LMM is a proven method for modeling the sine-sweep test with an acceleration base input [43]. In this method a large mass (m, more than seven orders larger than the total mass of the skin) was added at the point of input, and a harmonic force ($F^n = m \cdot A^n$) was applied that creates the desired acceleration load. In this study, a large mass (1.0×10^{30} kg) was used with its translational DOFs, which were coupled with those at each rivet joint as shown in Fig. 10, to replicate the base input transferred through these joints.

The phase angle plots can be obtained through the harmonic response analysis for each excitation frequency (f_e^1 and f_e^2) as shown in Fig. 11(a). In both excitation cases, the domain was clearly segmented. In the f_e^1 excitation case, the vicinity of each rivet joint has positive phase and the other region (including the center of plate) has nega-
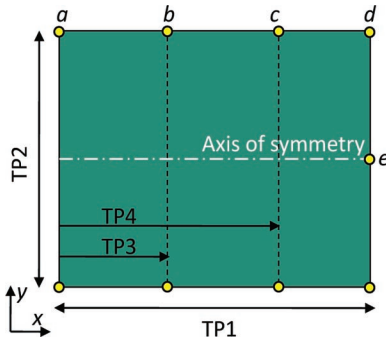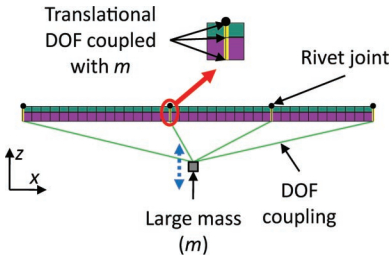

Fig. 8. First two mode shapes (modal analysis result).

Fig. 9. Tuning parameters for model tuning.

Fig. 10. Modeling of base excitation by the large mass method.
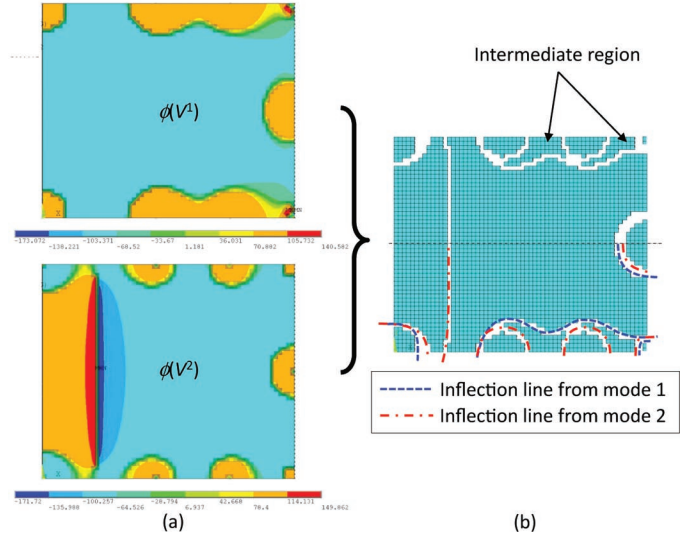

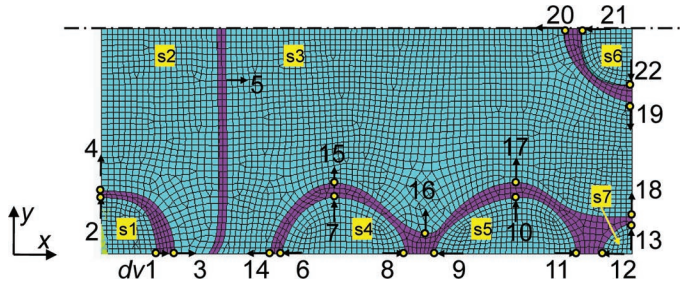Fig. 11. (a) Voltage phase angles from multiple modes and (b) inflection line elimination.

Fig. 12. FE model parameterization and indexes for shape design variables (dv_k) and segments (s_j). In this optimization step, voltage coupling conditions and external resistors were implemented for each PZT segment. Seven design variables on the resistor values (R_j, $j = 1, \ldots, 7$) were additionally defined. Therefore, 29 design variables were involved (22 for shape change, 7 for resistance values).

tive phase. In the $f_e{}^2$ excitation case, however, the center segment was divided into two sub-regions. A different segmentation around rivets b to d (see Fig. 9 for rivet index) was also generated: separate segments were generated for each rivet joint.

Fig. 11(b) shows the PZT layer segmentation created by removing inflection lines from multiple modes. The inflection lines around rivets a and e were almost identical in the two vibration modes. In the vicinity of rivets b to d, however, the inflection lines from the two modes did not agree and intermediate regions were generated between the lines. Considering the relatively low strain level, and thus small contribution to power generation, these regions were ignored for the model parameterization for the SO step. The central region was segmented along the vertical inflection line from the second mode.

4) Optimization of Shape and External Resistor: The shape optimization (SO) step was also performed, as was the optimization of the external resistors. The parameterized model is shown in Fig. 12. The model parameterization has been done using the morphing technique supported by Hypermesh (Altair Engineering Inc., Troy, MI) [44]. The design parameters were defined in the lower half of the model and the model's symmetry was assumed for the whole model (the axis of symmetry is shown in the figure). After removing PZT materials along the inflection lines and intermediate regions, the edges of PZT segments were smoothly remodeled using B-splines. The locations of control points were assigned as design variables (dv_k, $k = 1, \ldots, 22$) except dv_5, which is assigned to locate the vertical inflection line along the x axis. For more accurate

simulation result, the FE model was refined, with $14\,598$ elements in total. During the SO step, the material topology does not change and the number of segments is maintained.

The SO has been formulated as follows:

$$\max \sum_n \sum_j P_{nj}(dv_k, R_j)$$
$$\text{s.t.} \quad \max(\varepsilon_{\text{von}}) \leq \varepsilon_{\text{yield}} \qquad (9)$$
$$lb_k \leq dv_k \leq ub_k,$$

where P_{nj} is the power from jth segment (s_j, $j = 1, \ldots, 7$, as shown in Fig. 12) under nth mode excitation, dv_k is kth design variable with the bounds (lb_k, ub_k), $\max(\varepsilon_{\text{von}})$ is the maximum von-Mises strain of PZT material, $\varepsilon_{\text{yield}}$ is the allowable strain of PZT which is set as 500μ [17]. Initially all dv_k were set to zero, and the bounds were set as the maximum perturbation of dv_k which does not generate a negative Jacobian of a FE element, as shown in Table III.
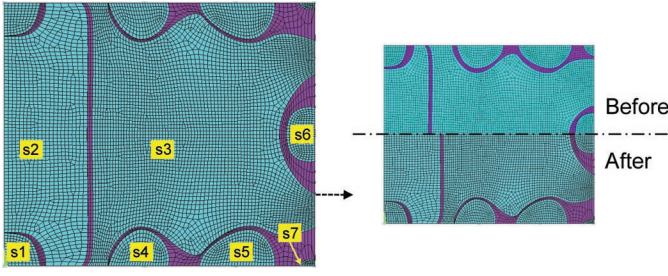
Fig. 13. Design optimization result and comparison with initial model.

Assuming the weak coupling between R_j and dv_k on the total power output, a stepwise design optimization strategy was proposed using (10) to promote fast convergence:

$$\max \sum_n \sum_j P_{nj}(R_j, dv_k) \Rightarrow \begin{cases} \max \sum_n \sum_j P_{nj}(R_j) \\ \downarrow \\ \max \sum_n \sum_j P_{nj}(dv_k). \end{cases} \quad (10)$$

As explained in Section II-B, the initial values for R_j were set as in (7). After the first step of optimization, the optimal resistance values (R_j^*) were obtained as listed in Table IV. The resistances for the s_3 and s_7 segments have the minimum and maximum values, where the maximum and minimum A_j are respectively found from the 7 segments.

As the second step, the optimum dv_k values were found as shown in Fig. 13. The final design was obtained after 28 iterations to generate 1.55 mW from both modes and the strain constraint was satisfied [the maximum value was about 27μ, which is far less than its limit $(\varepsilon_{\text{yield}})$]. The optimization result shows that the material on the left yielded higher efficiency based on the following (see Fig. 13): 1) the gap width was narrowed on the left (near s_1) and widened moving toward the right side of the model (s_6, s_7), 2) the inflection line between s_2 and s_3 moved rightward, and 3) s_4 and s_5 were relocated to the left.

Fig. 14(a) shows the improvement of the objective function (total power generation) during the shape optimiza-

tion. After 28 iterations, the optimal design was obtained to generate 1.55 mW. The SO step improves power generation by about 3.0% compared with the TO result. The power improvement on each segment was analyzed in Fig. 14(b). Even though there was a power decrease in s_3, the total power has been increased [as shown in Fig. 14(a)] because of the major power increase in s_2 segment. The power generation from the segments near each rivet joint $(s_1, s_4, s_5, s_6, s_7)$ was very small.

The harmonic response at each excitation frequency is shown in Fig. 15 with the amplitude of open-circuit voltage (V_{oc}) at each segment. In the first mode, the maximum $|V_{\text{oc}}|$ was discovered at s_2 because it had a larger strain than any other segments [Fig. 15(a)], whereas s_3 shows the largest $|V_{\text{oc}}|$ in the second mode [Fig. 15(b)]. V_{oc}s in small segments $(s_1, s_4, s_5, s_6, s_7)$ have different sign from the neighboring larger segments (s_2, s_3), indicating that voltage cancellation is eliminated by appropriate segmentation.

5) Discussion of Power Improvement: The performance improvement of the multimodal EH skin was summarized in Table V in which the power generation per unit acceleration $(1g)$ was compared for the three different cases: no segmentation (Case 0), segmentation considering the first mode only (Case 1, entitled unimodal EH skin), and multimodal EH (Case 2). Rows (a) and (b) indicate the power generation when each case is excited at frequencies f_e^1 and f_e^2, respectively. The more segmentation we implement according to the design rule suggested in this paper, the more power the EH skin generated, as shown in Table V. When the design is changed from Case 0 to Case 1, the power level increased significantly for the both modes (22.2 and 33.8%). It is concluded that the segmentation near the fixed rivet joints contributes to the power improvement in both modes. When Case 1 and Case 2 are compared, the power is mainly increased in the second mode (29.7%). It indicates that the elimination of the vertical inflection line (across the width of the skin) mainly contributes to power increase for the second mode. In summary, greater power generating performance of the multimodal EH skin (Case 2) was clearly proven.

TABLE III. Design Bounds for dv_k.

k	1	2	3	4	5	6	7	8	9	10	11
lb_k (mm)	−1.0	−0.5	−1.0	−0.5	−2.0	−1.0	−1.0	−5.0	−1.0	−5.0	−5.0
ub_k (mm)	1.0	0.5	1.0	0.5	7.0	1.5	1.0	1.0	1.5	1.0	1.0
k	12	13	14	15	16	17	18	19	20	21	22
lb_k	−4.0	−4.0	−1.0	−0.5	−0.5	−0.5	−0.5	−1.0	−1.0	−2.0	−2.0
ub_k	1.0	1.0	5.0	3.0	3.0	7.0	7.0	7.0	7.0	0.2	0.2

TABLE IV. R_j^* in the First Step.

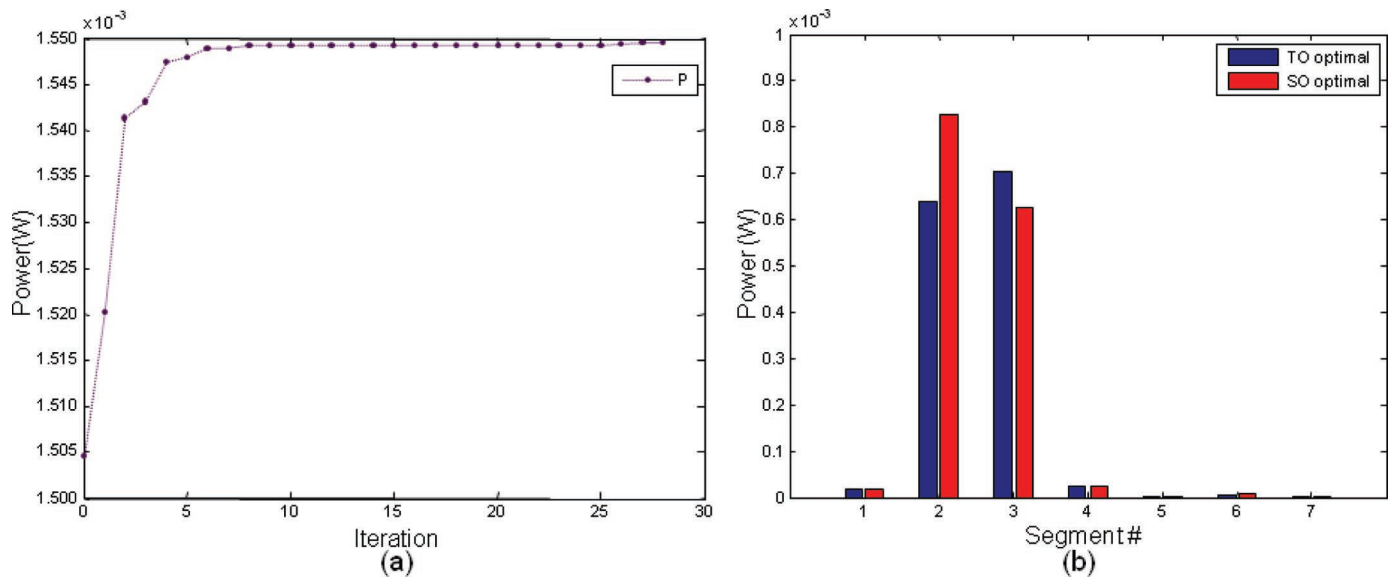| Segment	1	2	3	4	5	6	7
R_j^* (kΩ)	123.0	8.9	2.3	61.9	41.2	42.9	458.0

Fig. 14. (a) Design optimization history for power and (b) power improvement for each segment.
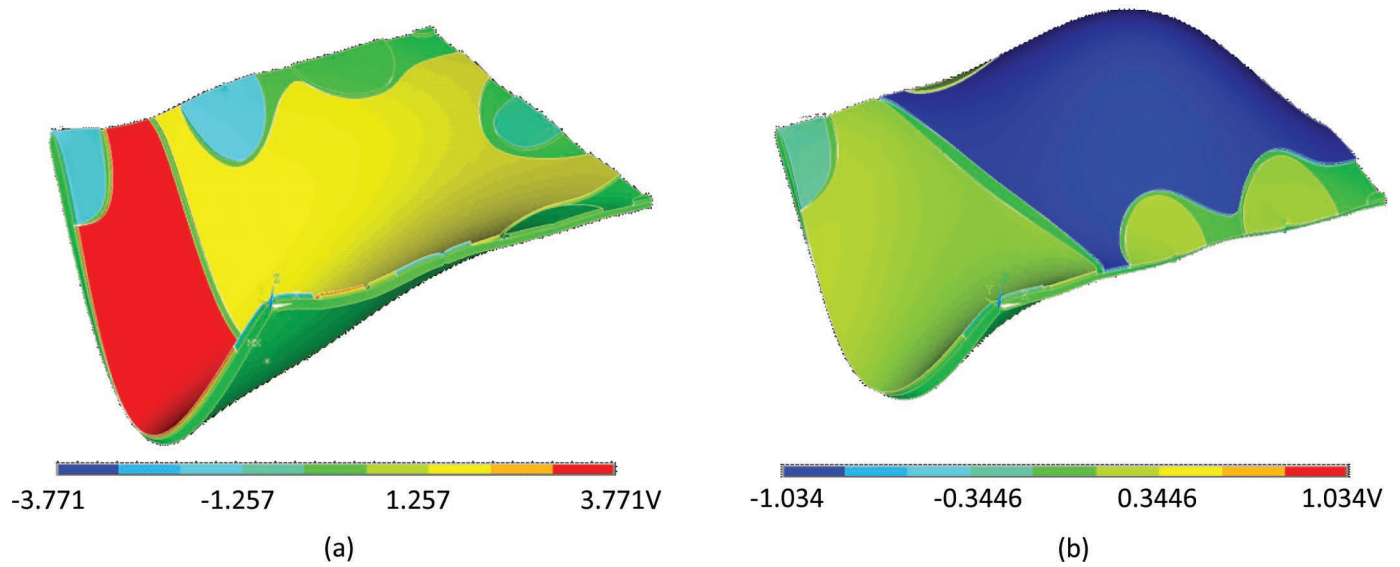
Fig. 15. Vibration shapes and V_{oc} by harmonic analysis: (a) first mode and (b) second mode.

TABLE V. POWER COMPARISON FOR DIFFERENT SEGMENTATION.

		Case 0		Case 1 (unimodal EH skin)		Case 2 (multimodal EH skin)
Power per unit	(a) at f_e^1	1.479	+22.2% →	1.807	+1.6% →	1.836
acceleration (mW/g)	(b) at f_e^2	0.136	+33.8% →	0.182	+29.7% →	0.236

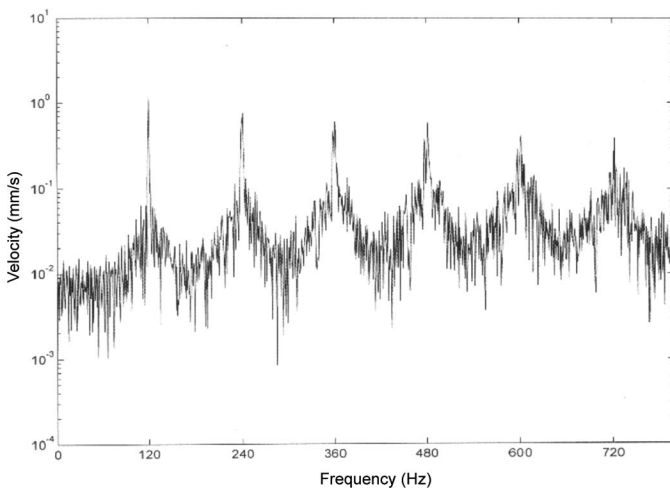Fig. 16. Power transformer (exterior view and interior windings).

Fig. 17. Vibration data in the transformer [47].

B. Case Study 2: Utilization of Power Transformer Vibration

1) Motivation of EH Skin Design for Power Transformer: The second case study involved vibration of a power transformer. Power transformers are among the most expensive elements in a power plant facility. The major role of the transformer is to increase voltage before transmitting electrical energy over long distances through wires. The alternating magnetic field causes fluctuating electromagnetic forces in the windings (see Fig. 16) and they produce harmonic vibration in the transformer. Fig. 17 shows an example of harmonic frequencies measured on the external surface of a transformer. Radiator fins are installed on the outside wall to aid the dissipation of heat and prevent winding insulation damage.

Online health monitoring of power transformers enables condition-based maintenance, resulting in a significant reduction of maintenance costs [44] and prevention of unexpected power supply stoppage, and economic and social losses. Most mechanical system failures of the transformers occur because of the severe vibration of the magnetic core, which causes transitory overloads on the windings [45]. Because of the difficulties of direct measurement inside the transformer, sensory data are obtained through indirect measurements on the exterior surface [46].

Much more than just avoiding the cost of wire, wireless sensors have recently received a great deal of attention, promising the ability to monitor structures in an easier and more affordable manner. One of the bottlenecks for implementation of wireless sensors is high maintenance cost, especially for battery replacement—the labor cost is extremely high because the extremely high voltage around transformers may lead to a fatal accident. This research has been motivated, therefore, to build a self-powering sensor network environment for transformers which does not require battery-replacement maintenance for the lifetime of the transformers.

2) Vibration Behavior of Power Transformer: As indicated in Section II, the proposed design method uses a computational model, so it is necessary to accurately analyze the vibrational behavior of the transformer. In this case study, a finite element model for the transformer has been constructed using ANSYS as shown in Fig. 18. This figure shows the FE model composed of internal 3 windings, supporting structures, and exterior walls with radiation ribs. The dimensions of the transformer are also shown in Fig. 18. The transformer walls are 15 mm thick, made of cast steel. Copper was chosen for the material of the windings. In total, 27 972 SOLID45 elements were used for the modeling. The fixed boundary condition was applied at the bottom surface of the transformer. The material properties of copper and cast steel are listed in Table VI.

The resonant frequencies of the transformer close to any of harmonic excitation frequency ($f_e^n = n \times 120$ Hz, as shown in Fig. 17) are critical factors in the amplifica-
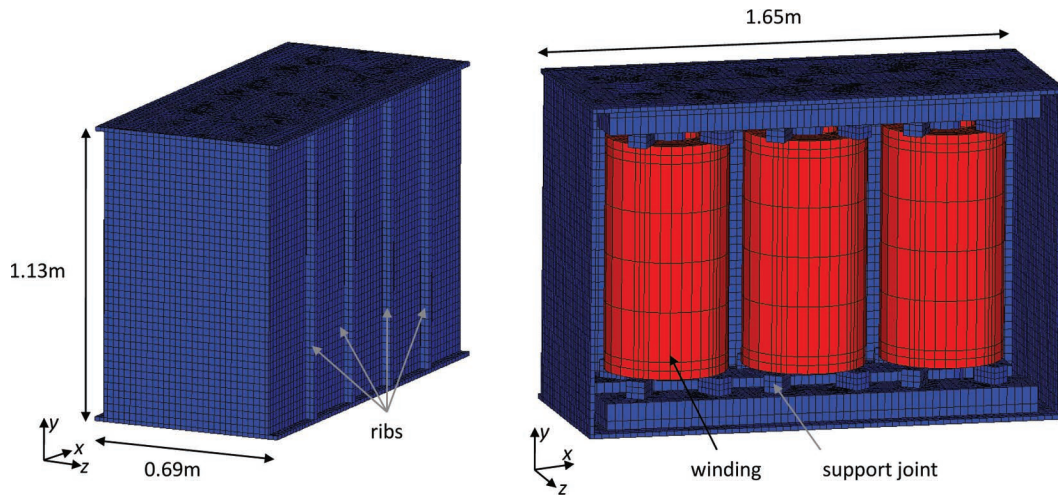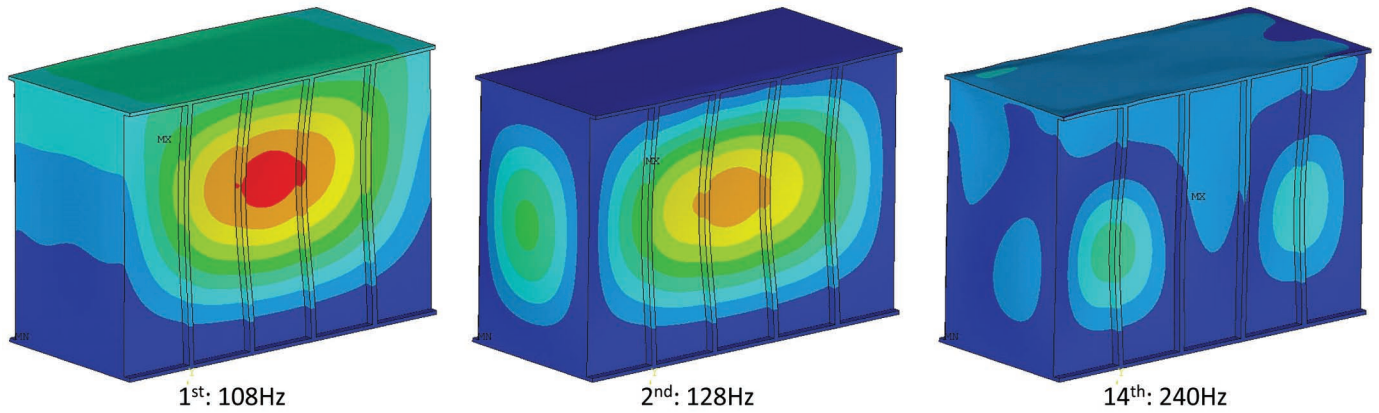
Fig. 18. FE model for a three-phase power transformer.

Fig. 19. Mode shapes near the harmonic excitation frequencies.

TABLE VI. Material Properties for Power Transformer Modeling.

Material	Parameter	Value
Cast steel	ρ_a	7850 kg/m^3
	Y_a	200 GPa
	ν_a	0.27
Copper	ρ_a	8960 kg/m^3
	Y_a	12.8 GPa
	ν_a	0.34

tion of excited vibrations, so the resonant frequency values were examined by modal analysis. The first 20 resonant frequencies were calculated as shown in Table VII and the modal shape near the first two harmonic excitation frequencies ($n \times 120$ Hz, $n = 1, 2$) are shown in Fig. 19; as seen here, these modes have relatively large vibration amplitudes on the front and back panels.

The harmonic vibration behavior of the transformer, generated by fluctuating electromagnetic forces in the windings, was simulated using harmonic analysis. The electromagnetic forces in the windings were applied as the form of axial harmonic displacement (u^{in}). The radial displacement of the windings was ignored. Knowing that the axial displacements of the two side windings are identical [48], the calibration problem has been formulated to find the axial harmonic displacements of the middle winding (u_m^{in}) and two side windings (u_s^{in}) so that the maximum harmonic amplitude (d_{sum}) is consistent with the measured data in reference [47]: $d_{max} = v_{max}/2\pi f = 17.4(\text{mm}/\text{sec})/2\pi(120$ Hz$) = 23.1$ μm, or

$$\text{to find } u_m^{in}, u_s^{in}, \text{ minimize } \{\max(d_{sum}(u_m^{in}, u_s^{in}) - d_{max})\}^2. \tag{11}$$

TABLE VII. First 20 Resonant Frequencies of the Transformer.

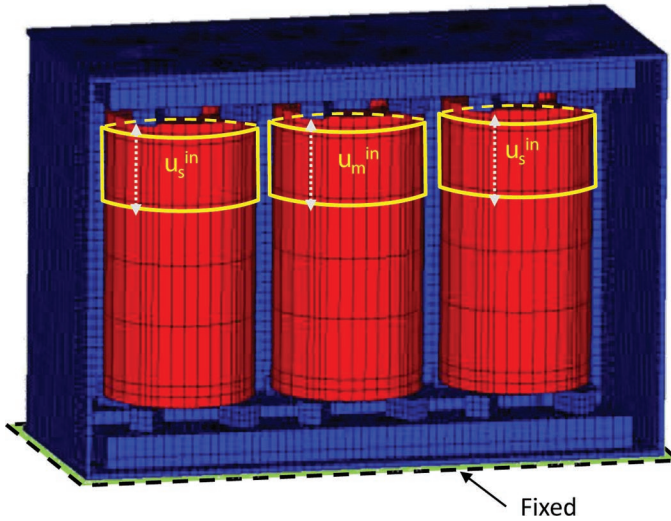| Mode	1	2	3	4	5	6	7	8	9	10
Freq. (Hz)	107.66	127.62	136.47	140.68	153.95	155.78	171.19	178.63	203.96	204.24
Mode	11	12	13	14	15	16	17	18	19	20
Freq.	219.23	223.89	234.05	240.27	262.48	263.65	265.19	274.05	289.18	292.51

Fig. 20. Loading and boundary conditions for harmonic analysis.

Fig. 20 shows the loading and boundary conditions for harmonic analysis. By minimizing the function defined in (11), $u_{\mathrm{s}}^{\mathrm{in}} = 3.0$ µm and $u_{\mathrm{m}}^{\mathrm{in}} = 1.2$ µm were obtained.

The harmonic analysis was performed at first two harmonic frequencies (120 and 240 Hz) because the harmonic vibration amplitude exponentially decreases from the third mode (360 Hz). The harmonic response in Fig. 21 is very similar to the modal shapes in Fig. 19. The front panel was chosen as the design space for EH skin because a larger strain level is expected based on its relatively larger vibration amplitude.

3) Topological Optimization: The multimodal EH skin design task introduced in Section II was applied to the transformer. The PZT-5A patches (1.02 mm thick. Material properties in Table II) covering the front panel were modeled using SOLID5 element in ANSYS. The volt

DOFs on the interface with the transformer panel were grounded ($V = 0$) as shown in Fig. 22. The voltage coupling condition at the exterior surface (representing exterior electrode) and the external resistors in Fig. 22 were implemented after eliminating inflection lines.

The method explained in Section II was used for inflection line detection. Fig. 23 shows the plots for the voltage phase angle and the corresponding inflection lines (dashed lines) at excitation frequencies f_{e}^1 and f_{e}^2. In both cases, the domain was clearly segmented. In both plots the blue (0°) and red (360°) part correspond to the same phase angle. (References to color refer to the online version of the figure.) In the f_{e}^1 excitation case, the plate was segmented as shown in the left of Fig. 23. The middle part has the phase around 0° and the phase was shifted into 180° near the top and bottom edges. In the f_{e}^2 excitation case, the layout of the inflection lines is more complex, having 6 segments in total.

Fig. 24 shows the PZT layer segmentation created by removing inflection lines. Fig. 24(a) shows the unimodal EH skin design (only the f_{e}^1 excitation case was considered); the multimodal EH skin design is shown in Fig. 24(b) (both f_{e}^1 and f_{e}^2 excitation cases were considered). In this stage, at each segment, the voltage DOFs for the nodes on the exterior PZT surface were coupled to represent an electrode. CIRCU94 elements were used to represent electrical resistors.

4) Optimization of External Resistors: The optimization problem of finding each resistor value for power maximization has been formulated as

$$\max \sum_{n=1,2} \sum_{j} P_{nj}(R_j), \qquad (12)$$

where P_{nj} is the power from jth segment at f_{e}^n excitation frequency (index j as shown in Fig. 24). The shape optimization was not performed in this case study because
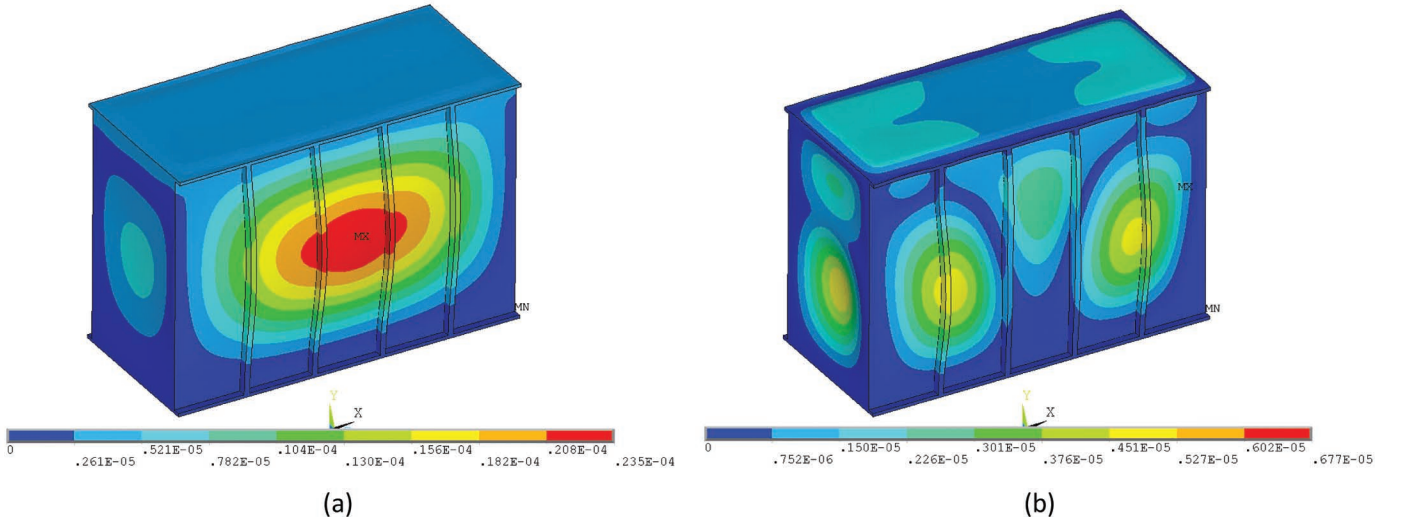

Fig. 21. Harmonic responses at each excitation frequency: (a) 120 Hz excitation, (b) 240 Hz excitation.
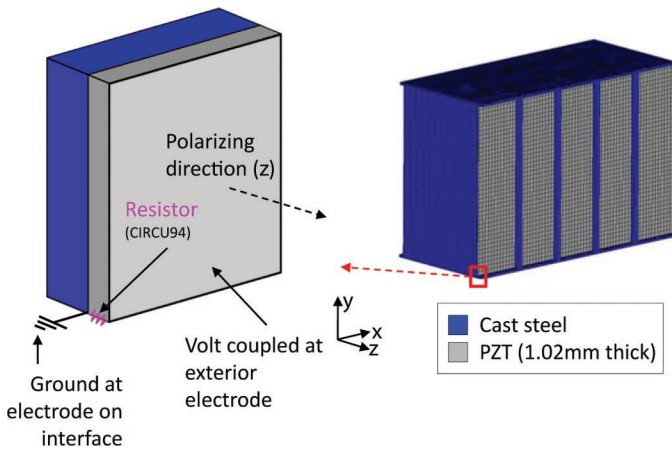
Fig. 22. Initial modeling of piezoelectric material before topology optimization.

of the high computational cost. The initial values for R_j were set by (7). The optimization results for the resistance values (R_j) are listed in Tables VIII and IX for unimodal and multimodal EH skin, respectively. The total power is 10.98 mW for the unimodal EH skin and 13.18 mW for the multimodal EH skin.

The segment-wise power output is displayed in Fig. 25. The power from the first and the second mode are indicated using red and blue bars, respectively, in the online version of the figure. Overall, the power enhancement from the second mode is clearly shown in the multimodal EH skin. When the largest center segments from each design are compared (7 in unimodal, 14 in multimodal EH skin), the power generation is similar between the two designs. When the second-largest segments are compared (4 and
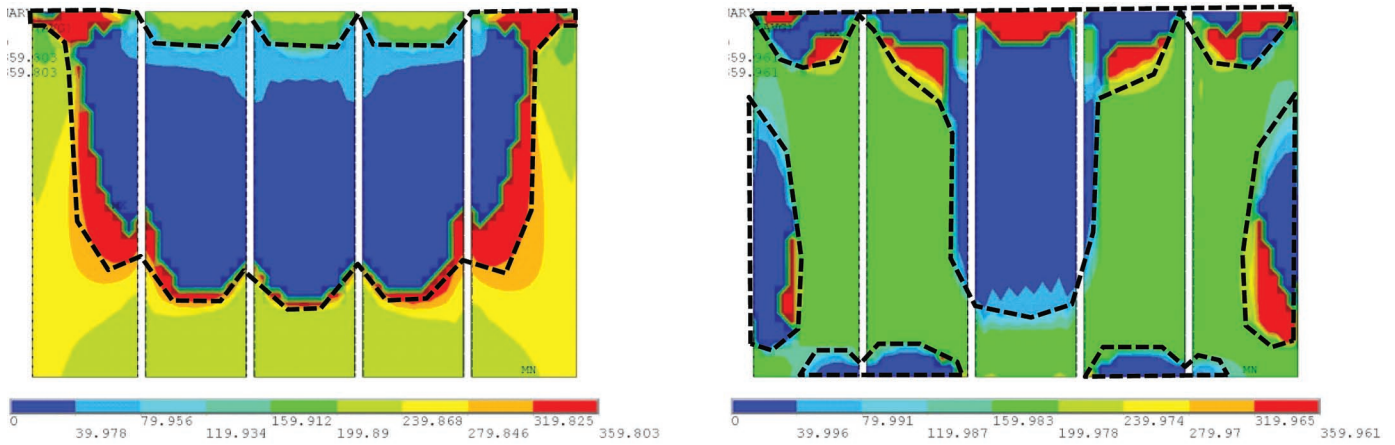
Fig. 23. Phase angle of open circuit voltage ($\phi(V_i)$) and inflection line layout at mode $i = 1, 2$.

(a)   (b)
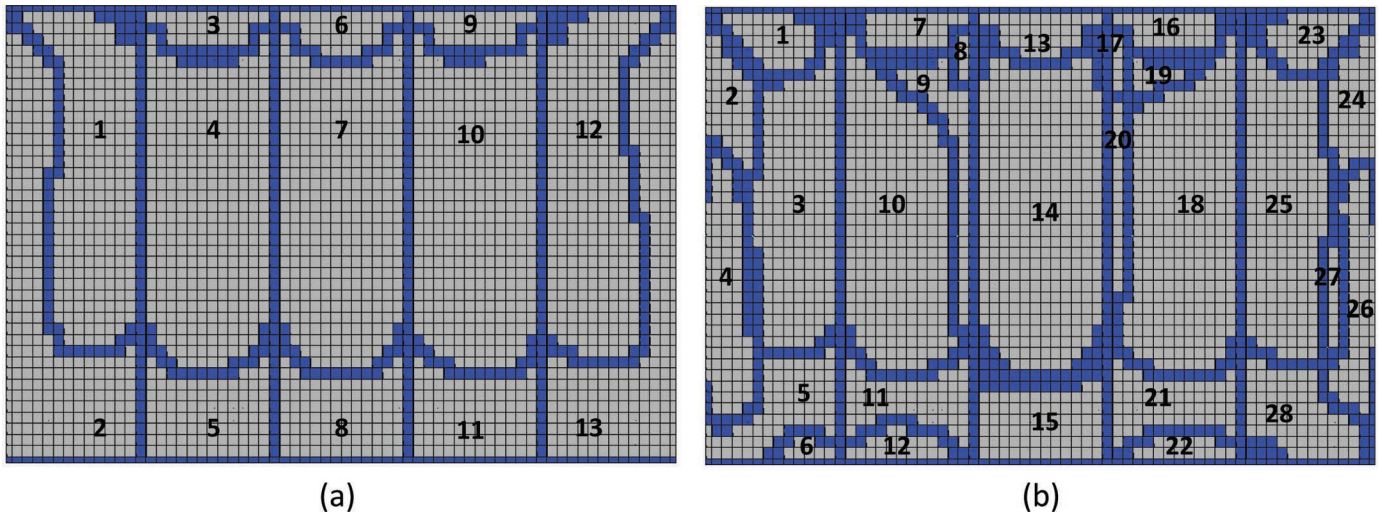
Fig. 24. Segment indexes for EH skin designs: (a) multimodal EH skin (1st and 2nd modes considered), (b) unimodal EH skin (1st mode considered).

TABLE VIII. Optimal R_J in Unimodal EH Skin.

Segment	1	2	3	4	5	6	7
R_j^* (kΩ)	0.58	0.53	4.61	0.41	1.42	4.03	0.40
Segment	8	9	10	11	12	13	
R_j^*	1.43	4.61	0.40	1.45	0.53	0.60	

Fig. 25. Comparison of segment-wise power generation: (a) unimodal EH skin, (b) multimodal EH skin.

TABLE IX. Optimal R_J in Multimodal EH Skin.

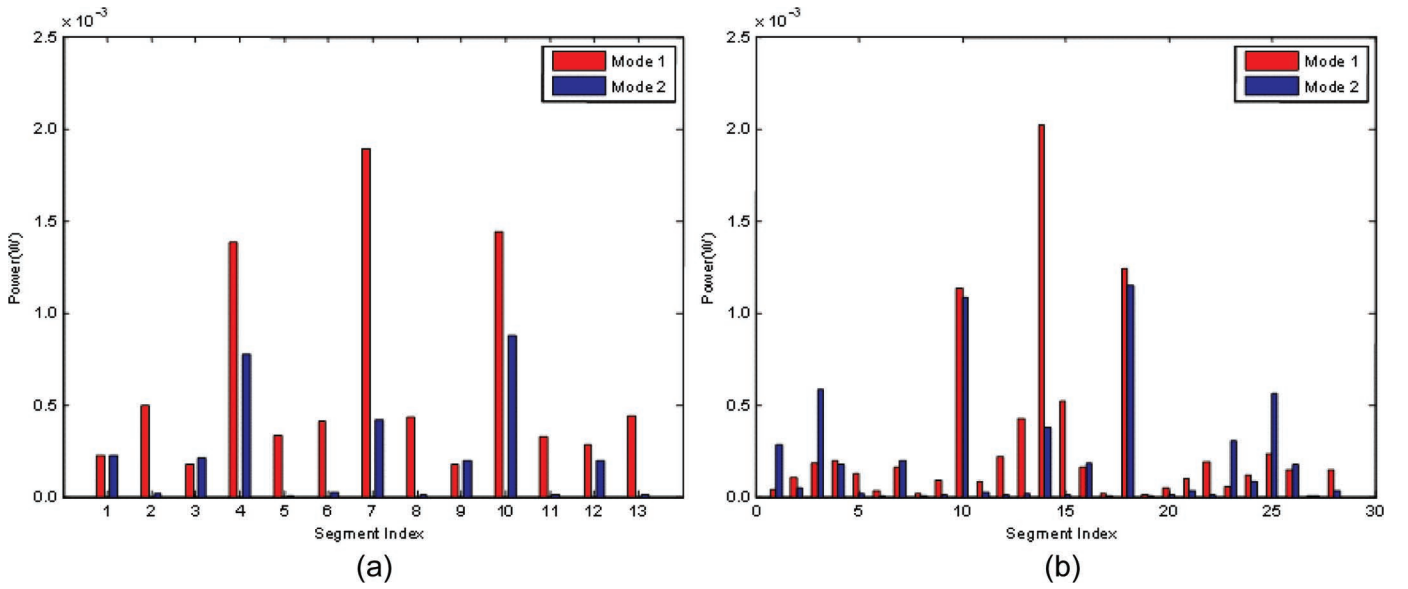| Segment	1	2	3	4	5	6	7
R_j^* (kΩ)	4.03	3.07	0.75	1.50	2.02	18.40	4.96
Segment	8	9	10	11	12	13	14
R_j^*	32.30	3.40	0.54	2.35	6.79	8.07	0.62
Segment	15	16	17	18	19	20	21
R_j^*	2.62	4.96	25.80	0.51	16.10	7.59	2.23
Segment	22	23	24	25	26	27	28
R_j^*	8.07	4.30	2.75	0.70	2.15	14.3	1.93

TABLE X. Comparison of Power Harvested.

Design	Unimodal		Multimodal	
Mode	1	2	1	2
Power (mW)	8.00	2.98	7.80	5.38
		10.98		13.18

10 in unimodal, 10 and 18 in multimodal), the multimodal design produces more power from the second mode even though the segment area is smaller. It is concluded that the cancellation effect in the segment of the unimodal design causes smaller power generation. However, segments 4 and 10 in the unimodal design produce more power from the first mode. Similar power generation phenomena are shown in segments 3 and 25 (multimodal EH skin) which produce larger power from the second mode than segments 1 and 12 (unimodal EH skin) for the same reason.

5) Discussion of Power Improvement: The amount of energy harvested from each design is analyzed in Table X. Basically, the unimodal design harvests more power from the first mode (8.00 mW) than the multimodal design (7.80 mW). Based on the fact that less PZT was used in the multimodal design, however, the performance of

the multimodal skin under the first mode excitation is comparable. Moreover, the advantage of the multimodal design is clearly shown in the second mode. Compared with the unimodal design (2.98 mW), there was an 81% increase of power harvested using the multimodal design (5.38 mW). For the total power harvested, the multimodal design harvests 13.18 mW, about 20% more than the unimodal design (10.98 mW). To summarize, the excellent power generating performance of multimodal EH skin was clearly proven.

The power improvement from the multimodal EH skin design can facilitate a larger number of wireless sensor operations. Considering the power requirement of a 3-axis wireless accelerometer (2.4 mW [9]), we can expect that the multimodal design can operate five accelerometers. The larger number of sensors will enhance the detection of failure modes [49] in the transformer and enable high-

reliability structural health monitoring and life prognostics. In practice the segments with small power generation in the multimode design (e.g., segments 6, 8, 17, 19, and 27) can be removed to reduce material usage.

IV. Conclusion

The new EH harvesting design concept, multimodal EH skin, was proposed for power generation from multiple harmonic vibration modes. The topological design of the multimodal EH skin was obtained by removing the PZT material along the inflection lines from multiple modal shapes to minimize the cancellation effect. The optimal external resistors at all segments were found using a design optimization algorithm for power maximization. The multimodal EH skin was compared with the skin without segmentation and the unimodal EH skin, and the superior performance of the multimodal EH skin was verified. Additional shape optimization may be followed for greater ease of manufacturing.

Even though this work is limited to simulation, the design of the EH skin proposed in this paper consists of thin composite layers and we can experimentally demonstrate the energy harvesting capability by simply attaching PZT patches using permanent glue such as epoxy. The implementation of the multimodal EH skin may include the following expected challenges. First, the design of the EH skin may be sensitive to boundary conditions. For instance, a change in rivet tightness in the aircraft skin may change the vibrational configuration (e.g., amplitudes, inflection line locations) and the optimal design of PZT material. Therefore, the sensitivity with respect to boundary conditions needs to be studied for the robust and reliable design of the EH skin. Second, a complex design layout caused by multiple segments may cause dense electrical wiring. To solve this problem, we may consider advanced wiring techniques such as conductive tape or silver pen, to avoid complicated wiring and maintain design compactness.

The proposed design principle for multimodal EH skin can be successfully applied to many engineered systems which have harmonically vibrating skins. In the near future, we plan to prove the versatility of the design concept with applications including structural health monitoring, building automation, etc., by integrating multimodal EH skin and wireless sensors.

Acknowledgments

References

[1] U.S. Department of Energy, (2008, Dec. 4) ITP sensors and automation: Low-cost vibration power harvesting for wireless sensors. [Online]. Available: http://www1.eere.energy.gov/industry/sensors_automation/pdfs/kcf_vibrationpower.pdf

[2] S. Roundy, P. K. Wright, and J. M. Rabaey, *Energy Scavenging for Wireless Sensor Networks: With Special Focus on Vibrations.* New York, NY: Springer, 2004.

[3] P. Glynne-Jones, S. P. Beeby, and N. M. White, "Towards a piezoelectric vibration-powered microgenerator," *IEE Proc. Sci. Meas. Technol.*, vol. 148, no. 2, pp. 68–72, 2001.

[4] M. G. Silk, *Ultrasonic Transducers for Nondestructive Testing*: Bristol, UK: Adam Hilger, 1984.

[5] T. Sterken, K. Baert, C. Van Hoof, R. Puers, G. Borghs, and P. Fiorini, "Comparative modeling for vibration scavengers," in *IEEE Sensors 2004*, 2004, pp. 1249–1252.

[6] K. Ren, Y. Liu, X. Geng, H. F. Hofmann, and Q. M. Zhang, "Single crystal PMN-PT/epoxy 1-3 composite for energy-harvesting application," *IEEE Trans. Ultrason. Ferroelectr. Freq. Control*, vol. 53, no. 3, pp. 631–638, 2006.

[7] N. Elvin, A. Elvin, and D. H. Choi, "A self-powered damage detection sensor," *J. Strain Anal. Eng. Des.*, vol. 38, no. 2, pp. 115–124, 2003.

[8] J. Nuffer and T. Bein, "Applications of piezoelectric materials in transportation industry," presented at *Proc. Global Symp. Innovative Solutions for the Advancement of the Transport Industry (TRANS-FAC)*, 2006.

[9] (2008, Jul. 24) Analog temperature sensor. AmbioSystem LLC, Heuvelton, NY, [Online]. Available: http://www.ambiosystems.com/index.php/Sensors/Analog-temperature-sensor/Detailed-product-flyer.html

[10] J. Granstrom, J. Feenstra, H. A. Sodano, and K. Farinholt, "Energy harvesting from a backpack instrumented with piezoelectric shoulder straps," *Smart Mater. Struct.*, vol. 16, no. 5, pp. 1810–1820, 2007.

[11] E. S. Leland, E. M. Lai, and P. K. Wright, "A self-powered wireless sensor for indoor environmental monitoring," in *Wireless Networking Symp.*, Austin, TX, 2004 [CD-ROM].

[12] Y. B. Jeon, R. Sood, J. Jeong, and S. G. Kim, "MEMS power generator with transverse mode thin film PZT," *Sens. Actuators A*, vol. 122, no. 1, pp. 16–22, 2005.

[13] G. Park, T. Rosing, M. D. Todd, C. R. Farrar, and W. Hodgkiss, "Energy harvesting for structural health monitoring sensor networks," *J. Infrastruct. Syst.*, vol. 14, no. 1, pp. 64–79, 2008.

[14] H. Bai, M. Atiquzzaman, and D. Lilja, "Wireless sensor network for aircraft health monitoring," in *Proc. 1st Int. Conf. Broadband Networks (BroadNets' 04)*, 2004, pp. 748–750.

[15] S. Roundy, P. K. Wright, and J. Rabaey, "A study of low level vibrations as a power source for wireless sensor nodes," *Comput. Commun.*, vol. 26, no. 11, pp. 1131–1144, 2003.

[16] F. Goldschmidtboeing and P. Woias, "Characterization of different beam shapes for piezoelectric energy harvesting," *J. Micromech. Microeng.*, vol. 18, no. 10, art. no. 104013, 2008.

[17] S. Roundy, E. S. Leland, J. Baker, E. Carleton, E. Reilly, E. Lai, B. Otis, J. M. Rabaey, P. K. Wright, and V. Sundararajan, "Improving power output for vibration-based energy scavengers," *IEEE Pervasive Comput.*, vol. 4, pp. 28–36, Jan-Mar. 2005.

[18] B. Zheng, C. J. Chang, and H. C. Gea, "Topology optimization of energy harvesting devices using piezoelectric materials," *Struct. Multidiscip. Optim.*, vol. 38, no. 1, pp. 17–23, 2009.

[19] E. C. N. Silva, "Comment on "Topology optimization of energy harvesting devices using piezoelectric materials," *Struct. Multidiscip. Optim.*, vol. 39, no. 3, pp. 337–338, 2009.

[20] A. Erturk and D. J. Inman, "Issues in mathematical modeling of piezoelectric energy harvesters," *Smart Mater. Struct.*, vol. 17, no. 6, art. no. 065016, 2008.

[21] H. Kim, Y. Tadesse, and S. Priya, "Piezoelectric energy harvesting," in *Energy Harvesting Technologies*, S. Priya and D. J. Inman, Eds. New York, NY: Springer, 2009, pp. 9–16.

[22] D. Shen, S. Y. Choe, and D. J. Kim, "Analysis of piezoelectric materials for energy harvesting devices under high-g vibrations," *Jpn. J. Appl. Phys.*, vol. 46, no. 10A, pp. 6755–6760, 2007.

[23] S. Lee, B. D. Youn, and B. C. Jung, "Robust segment-type energy harvester and its application to a wireless sensor," *Smart Mater. Struct.*, vol. 18, no. 9, art. no. 095021 2009.

[24] Y. Tadesse, S. Zhang, and S. Priya, "Multimodal energy harvesting system: piezoelectric and electromagnetic," *J. Intell. Mater. Syst. Struct.*, vol. 20, no. 5, p. 625–632, 2009.

[25] A. Kasyap, J. Lim, D. Johnson, S. Horowitz, T. Nishida, K. Ngo, M. Sheplak, and L. Cattafesta, "Energy reclamation from a vibrating piezoceramic composite beam," in *9th Int. Congr. Sound and Vibration (ICSV9)*, 2002.

[26] G. K. Ottman, H. F. Hofmann, A. C. Bhatt, and G. A. Lesieutre, "Adaptive piezoelectric energy harvesting circuit for wireless remote power supply," *IEEE Trans. Power Electron.*, vol. 17, no. 5, pp. 669–676, 2002.

[27] S. Meninger, J. O. Mur-Miranda, R. Amirtharajah, A. Chandrakasan, J. H. Lang, and C. Mit, "Vibration-to-electric energy conversion," *IEEE Trans. Very Large Scale Integr. (VLSI) Syst.*, vol. 9, no. 1, pp. 64–76, 2001.

[28] M. J. Guan and W. H. Liao, "On the efficiencies of piezoelectric energy harvesting circuits towards storage device voltages," *Smart Mater. Struct.*, vol. 16, no. 2, pp. 498–505, 2007.

[29] C. J. Rupp, A. Evgrafov, K. Maute, and M. L. Dunn, "Design of piezoelectric energy harvesting systems: A topology optimization approach based on multilayer plates and shells," *J. Intell. Mater. Syst. Struct.*, vol. 20, no. 16, p. 1923–1939, 2009.

[30] S. R. Anton and H. A. Sodano, "A review of power harvesting using piezoelectric materials (2003-2006)," *Smart Mater. Struct.*, vol. 16, no. 3, p. R1–R21, 2007.

[31] H. A. Sodano, D. J. Inman, and G. Park, "A review of power harvesting from vibration using piezoelectric materials," *Shock Vib. Dig.*, vol. 36, no. 3, pp. 197–205, 2004.

[32] S. Lee, B. D. Youn, and M. Giraud, "Designing energy harvesting skin structure utilizing outdoor unit vibration," in *ASME Int. Design Engineering Technical Conf. & Computers and Information in Engineering Conf.*, Montreal, Canada, 2010, art. no. DETC2010–29180.

[33] H. Allik and T. J. R. Hughes, "Finite element method for piezoelectric vibration," *Int. J. Numer. Methods Eng.*, vol. 2, no. 2, pp. 151–157, 1970.

[34] A. Badel, D. Guyomar, E. Lefeuvre, and C. Richard, "Efficiency enhancement of a piezoelectric energy harvesting device in pulsed operation by synchronous charge inversion," *J. Intell. Mater. Syst. Struct.*, vol. 16, no. 10, pp. 889–901, 2005.

[35] A. Erturk, P. A. Tarazaga, J. R. Farmer, and D. J. Inman, "Effect of strain nodes and electrode configuration on piezoelectric energy harvesting from cantilevered beams," *J. Vib. Acoust.*, vol. 131, no. 1, art. no. 011010, 2009.

[36] S. N. Chen, G. J. Wang, and M. C. Chien, "Analytical modeling of piezoelectric vibration-induced micro power generator," *Mechatronics*, vol. 16, no. 7, pp. 379–387, 2006.

[37] F. Lu, H. P. Lee, and S. P. Lim, "Modeling and analysis of micro piezoelectric power generators for micro-electromechanical-systems applications," *Smart Mater. Struct.*, vol. 13, no. 1, pp. 57–63, 2004.

[38] J. H. Lin, X. M. Wu, T. L. Ren, and L. T. Liu, "Modeling and simulation of piezoelectric MEMS energy harvesting device," *Integr. Ferroelectr.*, vol. 95, no. 1, pp. 128–141, 2007.

[39] A. Erturk and D. J. Inman, "An experimentally validated bimorph cantilever model for piezoelectric energy harvesting from base excitations," *Smart Mater. Struct.*, vol. 18, no. 2, art. no. 025009, 2009.

[40] (2010, Jan. 22) 2024 T3 Alclad Aluminum Sheet and Coil. Airparts, Inc., Kansas City, KS. [Online]. Available: http://www.airpartsinc.com/shopexd.asp?id=208

[41] (2008, Feb. 22) Catalog #7C, Piezo Systems, Inc., Woburn, MA. [Online]. Available: http://piezo.com/catalog7C.pdf

[42] (2009, Dec 12) Alclad Aluminum 7075-O, MatWeb Material Property Data. [Online]. Available: http://www.matweb.com/search/DataSheet.aspx?MatGUID=7d7d6e4e0bf74145800cae70b5e96314&ckck=1

[43] D. Haberman, (2008, Apr. 24) Sine-sweep test simulation. [Online]. Available: http://ansys.net/tips/week6-compar-lm-dd3.pdf

[44] T. Leibfried and A. G. Siemens, "Online monitors keep transformers in service," *IEEE Comput. Appl. Power*, vol. 11, no. 3, pp. 36–42, 1998.

[45] D. Allan, M. Blundell, K. Boyd, and D. Hinde, "New techniques for monitoring the insulation quality of in-service HV apparatus," *IEEE Trans. Electr. Insul.*, vol. 27, no. 3, pp. 578–585, 2002.

[46] H. L. Rivera, J. A. Garcia-Souto, and J. Sanz, "Measurements of mechanical vibrations at magnetic cores of power transformers with fiber-optic interferometric intrinsic sensor," *IEEE J. Sel. Topics Quantum Electron.*, vol. 6, no. 5, pp. 788–797, 2000.

[47] W. R. Lee and J. S. Lee, "Study on vibration velocity rating for main transformer in nuclear power plant," in *Korean Soc. Noise and Vibration Engineering (KSNE) Annu. Spring & Fall Conf.*, 2005, pp. 587–594. (in Korean)

[48] H. Peter, H. Andreas, K. Manfred, B. Florian, D. Markus, I. Hans, and H. Alexander, "3D-FEM simulation for investigation of load noise of power transformers verified by measurements," in *2008 Int. Conf. Electrical Machines*, Vilamoura, Portugal, pp. 1–4.

[49] P. Wang, B. D. Youn, and C. Hu, "A generic sensor network design framework based on a detectability measure," in *ASME Int. Design Engineering Technical Conf. & Computers and Information in Engineering Conf.*, Montreal, Canada, 2010, art. no. DETC2010–29181.

Soobum Lee received his Ph.D. degree from the department of Mechanical Engineering at the Korea Advanced Institute of Science and Technology (KAIST), Korea, in 2007. Currently, he is a postdoctoral research associate at the department of Aerospace and Mechanical Engineering in the University of Notre Dame, Notre Dame, IN. His main research interests include energy harvester design, topology optimization, structural design for nuclear plant systems, robust design, and reliability-based design optimization. Dr. Lee is an author of more than 20 refereed journal articles in the field of design optimization and energy harvesting. He won the best paper prize in the division of CAE and computational mechanics by the Korean Society of Mechanical Engineering (KSME) in 2007, and was awarded a highlight of collections by *Smart Materials and Structures* in 2009.

Byeng D. Youn received his Ph.D. degree from the department of Mechanical Engineering at the University of Iowa, Iowa City, IA, in 2001. He was a research associate at the University of Iowa (until 2004), an assistant professor in Michigan Technical University (until 2007), and an assistant professor in the University of Maryland College Park (until 2010). Currently, he is an assistant professor at the School of Mechanical and Aerospace Engineering at Seoul National University, Republic of Korea. His research is dedicated to well-balanced experimental and simulation studies of system analysis and design, and he is currently exploring three research avenues: system-risk-based design, prognostics and health management (PHM), and energy harvester design. Dr. Youn's research and educational dedication has led to: six notable awards, including the ISSMO/Springer Prize for the Best Young Scientist in 2005 from the International Society of Structural and Multidisciplinary Optimization (ISSMO), and more than 100 publications in the area of system-risk-based design and PHM and energy harvester design.